AAS 24-196

SMALL BODY SLAM WITH SILHOUETTE-BASED GAUSSIAN PROCESS BATCH FILTERING

Quinn P. Moon,[*] Brandon A. Jones,[†] Ryan P. Russell,[‡] Courtney Hollenberg,[§] Daniel P. Lubey,[§] Shyam Bhaskaran[§]

Recent small body missions have successfully utilized Stereo-Photoclinometry (SPC) to model the shape of small bodies for landmark-relative navigation. To simplify estimation for onboard, autonomous implementation, the small body's shape is modeled using a Gaussian Process (GP), where multiple basis nodes and basis radii are used to predict the entire shape. The GP methodology was previously implemented into an Iterative Extended Kalman Filter (IEKF) for Simultaneous Localization and Mapping (SLAM) of the small body Eros. The IEKF was proven to be successful, yet sensitive to initial state estimates and errors. Thus a maximum-likelihood, GP batch least-squares algorithm is developed where conservative initial conditions are utilized. Simulated images of Eros are processed to extract the visible horizon and associated to a truth and estimated GP shape model. Through multiple batch iterations with a declining measurement under-weighting scheme, the GP batch algorithm estimates the body's shape to within meters of error, while also estimating the body's orientation, the body's spin rate, and the satellite's position and velocity. The GP batch algorithm is tested on a circular orbit and a hyperbolic approach trajectory for various small bodies. The GP batch implementation itself is a powerful tool for small body mapping and navigation, but subsequent work will focus on using the final state estimate and covariance from the batch filter as initial conditions for perturbing the truth states within a Monte Carlo study of the IEKF.

INTRODUCTION

The process of modeling a small body's shape and terrain through shadowed images, or Stereo-Photoclinometry (SPC), is a proven method for mapping and relative terrain navigation[1,2] in a variety of missions, including the Dawn mission to Ceres and Vesta[3,4] and the OSIRIS-REx mission to Bennu.[5] However, SPC is computationally intensive and requires considerable human interaction, and thus not well suited as an onboard capability. Autonomous algorithms are desired such that a spacecraft can approach a small body and through Simultaneous Localization and Mapping (SLAM) navigate and shape the body without relying on ground support. Silhouette-based measurements are readily produced by onboard visible spectrum cameras and are a cheap source of direct measurements of the central body's shape, ideal for autonomous SLAM applications. Additional work to advance the field of autonomous SLAM applications has been done through LIDAR imagery to

[*]PhD Student, Aerospace Engineering, University of Texas at Austin, Austin, TX, 78705; quinnpmoon@utexas.edu
[†]Associate Professor, Aerospace Engineering, University of Texas at Austin, Austin, TX, 78705; brandon.jones@utexas.edu
[‡]Professor, Aerospace Engineering, University of Texas at Austin, Austin, TX, 78705; ryan.russell@austin.utexas.edu
[§]Navigation Engineer, Outer Planet Navigation Group, Mission Design and Navigation Section, Jet Propulsion Laboratory, California Institute of Technology. 4800 Oak Grove Drive, Pasadena, California, 91109

track landmarks on Eros,[6] flash LIDAR imagery about Itokawa,[7] infrared imagery of Bennu,[8] and light-curve inversion.[9,10]

Recent work implemented a Gaussian Process (GP) to model a small body's shape with basis nodes and radii. Through GP regression, a tractable set of basis nodes and radii predicts the radius across the entire body. More basis nodes and radii used yield higher fidelity shape models, as depicted in illustration show in Fig. 1.

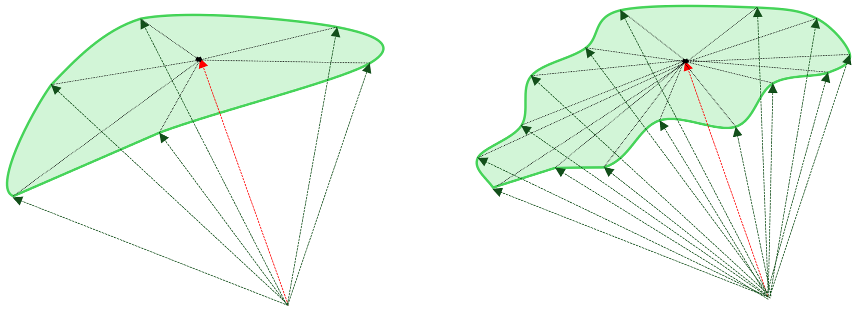

Figure 1: Shape Modeling with Gaussian Regression

Wahlstrom and Ozkan introduced a sequential GP estimation filter for target tracking,[11] and researchers from JPL and the University of Texas at Austin implemented the GP technique for small body mission analysis using silhouette-based measurements. An Iterative Extended Kalman Filter (IEKF) was developed to model the shape and pole of Eros,[12,13] and later successfully implemented in an IEKF SLAM algorithm to include the estimation of the spacecraft's position and velocity.[14]

A crucial aspect of an Extended Kalman Filter is validating the implementation and simulation model with a Monte Carlo study.[15] A proper Monte Carlo analysis requires the truth to be perturbed based on statistically consistent initial conditions. Particularly challenging for SLAM applications is perturbing the truth shape. The truth GP shape has sensitive spatial correlations defined by a covariance function, or kernel function, where points along the surface that are closer together are correlated more strongly. Furthermore, perturbations to the asteroid's radii are naturally bounded below, as the radii cannot be less than zero. Thus, the shape must be perturbed in a matter that is consistent with its radii, while also accounting for the spatial correlations.

To obtain the initial mean and covariance for future Monte Carlo studies, a maximum likelihood, batch least-squares algorithm is developed with the GP framework. The GP batch filter is derived and implemented to simultaneously estimate the spacecraft's position and velocity, and the central body's orientation, spin, and shape with only silhouette-based imagery. The details of the GP batch filter, the measurement equations, and data association process are provided. The GP batch filter is tested on a variety of mission scenarios, including for different asteroids and trajectories. The batch is specifically tested for a hyperbolic approach and a circular orbit about the asteroids Lutetia, Eros, Toutatis, and Bennu.

GAUSSIAN PROCESSES FOR ASTEROID SHAPE MODELING

The GP batch filter estimates the state vector

$$\boldsymbol{x} = \left[\begin{array}{ccccccc} \boldsymbol{r}^T & \boldsymbol{v}^T & \alpha & \delta & \dot{\theta} & \theta_0 & \boldsymbol{f}'^T \end{array} \right]^T, \tag{1}$$

where $\boldsymbol{r}$ and $\boldsymbol{v}$ denote the spacecraft's position and velocity with respect to the asteroid, α and δ the right ascension and declination of the asteroid axis of rotation, $\dot{\theta}$ the asteroid's spin about the prime meridian θ_0, and $\boldsymbol{f}'$ the basis radii of the asteroid at predetermined basis nodes $\hat{\boldsymbol{e}}'$. The basis nodes and radii are marked with a prime to distinguish between a measured radii and a basis radii.

The pole elements map the inertial frame to the asteroid frame using Euler angles according to the direction cosine matrix

$$\boldsymbol{T}_A^I = \boldsymbol{T}_3(\dot{\theta}t + \theta_0)\boldsymbol{T}_1(\tfrac{\pi}{2} - \delta)\boldsymbol{T}_3(\tfrac{\pi}{2} + \alpha), \tag{2}$$

where $\boldsymbol{T}_1$ and $\boldsymbol{T}_3$ with arbitrary input ϕ are:

$$\boldsymbol{T_1}(\phi) = \begin{bmatrix} 1 & 0 & 0 \\ 0 & \cos(\phi) & \sin(\phi) \\ 0 & -\sin(\phi) & \cos(\phi) \end{bmatrix}, \boldsymbol{T_3}(\phi) = \begin{bmatrix} \cos(\phi) & \sin(\phi) & 0 \\ -\sin(\phi) & \cos(\phi) & 0 \\ 0 & 0 & 1 \end{bmatrix}. \tag{3}$$

A GP is implemented as a regression technique to predict the asteroid's radii $\boldsymbol{f}$ at a measured node $\hat{\boldsymbol{e}}$ with a basis set. The basis set consists of unit nodes $\hat{\boldsymbol{e}}'$ and their associated radii $\boldsymbol{f}'$. Note that basis nodes and radii are distinguished from measured nodes and radii with a prime. From the basis set, the radii at any measured node $\hat{\boldsymbol{e}}$ is predicted according to the GP prediction equation:[16]

$$\boldsymbol{f}(\hat{\boldsymbol{e}}) = \boldsymbol{C}(\hat{\boldsymbol{e}}, \hat{\boldsymbol{e}}')\boldsymbol{C}^{-1}(\hat{\boldsymbol{e}}', \hat{\boldsymbol{e}}')\boldsymbol{f}(\hat{\boldsymbol{e}}'). \tag{4}$$

A significant benefit of GP regression lies in its ability to model and interpolate along the small body with a limited, discrete set of nodes. The entire shape of a small body can be encapsulated with just a few nodes and their kernel function, making it ideal for autonomous navigation. The "kernel trick" allows for complicated, multi-dimensional data to be represented more simply.[16] For shape modeling, the covariance function (kernel) correlates nodes through their angular distance according to

$$\boldsymbol{C}(\hat{\boldsymbol{e}}, \hat{\boldsymbol{e}}') = \sigma_f^2 \exp\left(-\frac{\arccos(\hat{\boldsymbol{e}}^T\hat{\boldsymbol{e}}')}{l^2}\right), \tag{5}$$

where correlation decays with increasing angular distance between two nodes. The kernel function takes two inputs, where each input can be either a measured node $\hat{\boldsymbol{e}}$ or a basis node $\hat{\boldsymbol{e}}'$. Nodes closer to each other have a stronger correlation, and nodes that are farther apart have a weaker correlation. The scaling factor l adjusts the strength of the spatial correlation, and σ_f^2 is an additional parameter, but here is set to unity.

Thus, the shape of an asteroid can be captured by a discrete set of nodes and radii. More nodes in the basis set increases the shape model fidelity, but slows down the filter as the number of state elements increases. Furthermore, a point of diminishing returns is quickly achieved when increasing the number of nodes, due primarily to fundamental observability limits associated to the nature of the silhouette-only measurements. All truth shape models implemented in the filter have 312 nodes obtained by performing a GP regression with a higher fidelity model as the basis set. The high fidelity shape models are obtained from NASA's Planetary Data System, pulled from Clark[17] and Hergenrother[18] for Bennu, Hudson[19] for Toutatis, Gaskell[20] for Eros, and Gaskell and Carry[21] for Lutetia.

There is a small yet crucial difference between the real shape of an asteroid and the GP filter truth shape. A useful comparison to understand this difference is through spherical harmonic gravity models. In a real-time mission, the gravitational acceleration is due to a complicated, high degree spherical harmonic model. The GRAIL mission estimated the gravity field of the Moon with thousands of Stokes' coefficients,[22] yet the gravity experienced in real time was due to, in theory, an infinite degree gravity model. Similarly, the shape of an asteroid can be thought of a GP shape with infinite basis nodes, converging to the truth shape of an asteroid.

The GP filter truth shape is modeled using 312 nodes, yet the images are captured from the real central body. Thus a data association procedure is run to convert the real-time image data to be representative of the 312 node shape model. Just as a real-time mission undergoes acceleration due to an infinite degree gravity model yet models the truth with a finite set of Stokes' coefficients. Figure 2 depicts a high fidelity polyhedral model of Eros and the GP filter truth shape. Note that the filter truth shape differs slightly from the polyhedral model, particularly on the extreme ends.

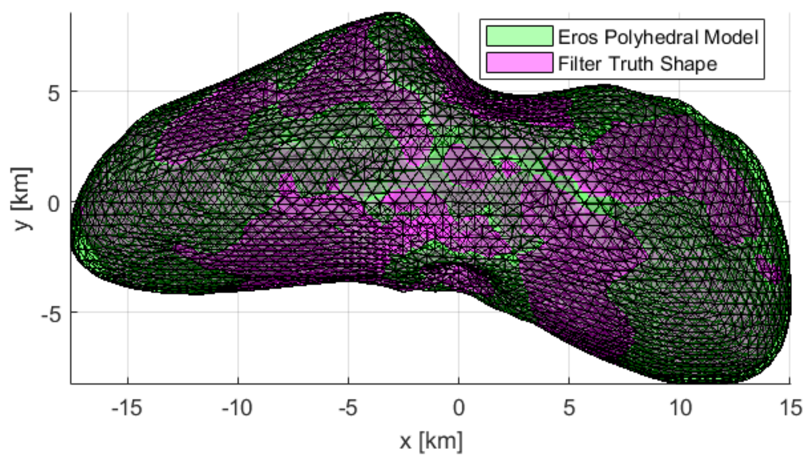

Figure 2: 312 Node Eros Truth Shape Models

Gaussian Process Batch Filter

The filter itself is derived from nonlinear maximum likelihood estimation. An arbitrary measurement function is expressed as

$$\boldsymbol{z} = \boldsymbol{h}(\boldsymbol{f}) + \boldsymbol{\epsilon}, \tag{6}$$

$$\delta\boldsymbol{z} = \boldsymbol{H_f}\delta\boldsymbol{f} + \delta\boldsymbol{\epsilon}, \tag{7}$$

where $\boldsymbol{H_f} = \frac{\partial \boldsymbol{h}}{\partial \boldsymbol{f}}$, and ϵ represents measurement noise. The augmented state is normally distributed according to:[14,16]

$$\begin{bmatrix} \boldsymbol{z} \\ \boldsymbol{f} \end{bmatrix} \sim \mathcal{N}\left(\begin{bmatrix} \boldsymbol{C}(\hat{e}, \hat{e}')\boldsymbol{C}^{-1}(\hat{e}', \hat{e}')\boldsymbol{f}(\hat{e}') \\ \boldsymbol{f}(\hat{e}') \end{bmatrix}, \begin{bmatrix} \boldsymbol{H_f}\boldsymbol{C}(\hat{e}, \hat{e})\boldsymbol{H_f}^T + \sigma_\epsilon^2 \boldsymbol{I} & \boldsymbol{H_f}\boldsymbol{C}(\hat{e}, \hat{e}') \\ \boldsymbol{C}(\hat{e}', \hat{e})\boldsymbol{H_f}^T & \boldsymbol{C}(\hat{e}', \hat{e}') \end{bmatrix} \right). \tag{8}$$

The covariance of $\boldsymbol{z}$ conditioned on $\boldsymbol{f}$ is[15]

$$\boldsymbol{P}_{\boldsymbol{z}|\boldsymbol{f}} = \boldsymbol{H}_{\boldsymbol{f}} \left(\boldsymbol{C}(\hat{e},\hat{e}) - \boldsymbol{C}(\hat{e},\hat{e}')\boldsymbol{C}^{-1}(\hat{e}',\hat{e}')\boldsymbol{C}(\hat{e}',\hat{e}) \right) \boldsymbol{H}_{\boldsymbol{f}}{}^T + \sigma_\epsilon^2 \boldsymbol{I}. \tag{9}$$

The GP batch algorithm is setup according to traditional batch least-squares algorithms,[23] estimating the state at the final time, with the GP components as derived by Wahlstrom and Ozkan.[11] The information matrix and state residuals are propagated forward and updated according to:

$$\boldsymbol{\mathcal{I}}(t_{k+1}) = \boldsymbol{\Phi}^T(t_k,t_{k+1})\boldsymbol{\mathcal{I}}(t_k)\boldsymbol{\Phi}(t_k,t_{k+1}) + \boldsymbol{H}^T(t_{k+1})\boldsymbol{W}(t_{k+1})\boldsymbol{H}(t_{k+1}), \tag{10}$$

$$\delta\boldsymbol{y}(t_{k+1}) = \boldsymbol{\Phi}^T(t_k,t_{k+1})\delta\boldsymbol{y}(t_k) + \boldsymbol{H}^T(t_{k+1})\boldsymbol{W}(t_{k+1})\left[\boldsymbol{z}(t_{k+1}) - \hat{\boldsymbol{z}}(t_{k+1})\right], \tag{11}$$

where the State Transition Matrix (STM) $\boldsymbol{\Phi}$ is propagated forwards along the reference trajectory and inverted using the symplectic properties of the STM.[24] The state and STM are propagated using 2-body relative gravitational motion. The measurement partial $\boldsymbol{H}$ with respect to all state elements is computed at the reference state and contains the sub-elements

$$\boldsymbol{H} = \left[\begin{array}{ccccccc} \boldsymbol{H}_{\boldsymbol{r}} & \boldsymbol{H}_{\boldsymbol{v}} & \boldsymbol{H}_\alpha & \boldsymbol{H}_\delta & \boldsymbol{H}_{\dot\theta} & \boldsymbol{H}_{\theta_0} & \boldsymbol{H}_{\boldsymbol{f}'} \end{array} \right]. \tag{12}$$

Note that $\boldsymbol{H}$ contains partials evaluated at the basis nodes $\frac{\partial \boldsymbol{h}}{\partial \boldsymbol{f}'}$, whereas Eq. 9 requires the measurement partials evaluated at the measured nodes. The weighting matrix $\boldsymbol{W}$ is calculated from the conditional covariance derived in Eq. 9 with measurement noise

$$\boldsymbol{W} = \left(\boldsymbol{P}_{\boldsymbol{z}|\boldsymbol{f}} + \boldsymbol{R} \right)^{-1}. \tag{13}$$

The truth measurements $\boldsymbol{z}$ remain constant over batch iterations, whereas the estimated measurements $\hat{\boldsymbol{z}}$ change over batch iterations. The final state update is calculated according to

$$\delta\boldsymbol{x}(t_{k_f}) = \boldsymbol{\mathcal{I}}^{-1}(t_{k_f})\delta\boldsymbol{y}(t_{k_f}), \tag{14}$$

and added to the estimate of the previous batch iteration, such that over batch iterations (denoted with subscript i) the final state estimate $\hat{\boldsymbol{x}}(t_{k_f})$ converges to the truth

$$\hat{\boldsymbol{x}}_{i+1}(t_{k_f}) = \hat{\boldsymbol{x}}_i(t_{k_f}) + \delta\boldsymbol{x}_{i+1}(t_{k_f}). \tag{15}$$

All matrix inverse operations are performed on positive definite matrices. As such, the Cholesky factorization is used for numerical accuracy.

The batch filter runs through multiple iterations on the same set of truth measurements. With more batch iterations, the estimated state converges to the truth state provided that the estimates are approximately within the linearized region. The initial information matrix is ideally set to the zero matrix, simulating a valid maximum likelihood scenario. However, due to numerical instability, the initial information is set to $\boldsymbol{\mathcal{I}}(t_k) = 1 \times 10^{-12}\boldsymbol{I}$.

SILHOUETTE-BASED MEASUREMENTS

Silhouette-based measurements (or horizon-based measurements) are generated by extracting points along the visible edge of an illuminated surface. Consider the Blender[25] simulated image of Eros in Fig. 3a.

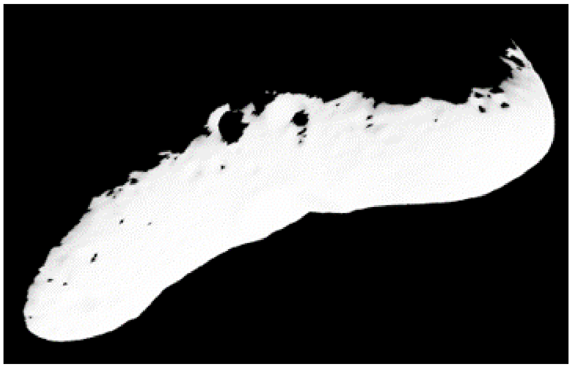

(a) Blender Simulated Image

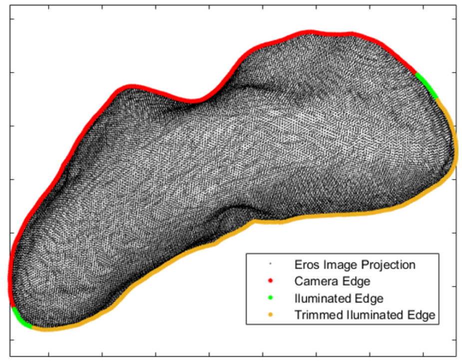

(b) MATLAB Simulated Images

For real time image extraction, an image processing tool is run on the image to find the boundary between illuminated and non-illuminated pixels. The longest continuous boundary corresponds to the visible edge; breaks in continuity are the result of self-shadowing and do not occur along the visible edge. A discrete set of points along the visible edge is extracted and incorporated as measurements. Only points along the visible edge are processed as measurements, as these are direct measurements of the asteroid's shape.

Previous work by Zucchelli[12] and Hollenberg[14] utilized Blender simulated images and extracted the visible edge with MATLAB's image processing toolbox. While the current batch filter also estimates the state successfully using the Blender images, relying on Blender to simulate different trajectories and asteroids is time consuming. As such, a boundary finding subroutine is utilized within MATLAB to extract the visible edge from the high fidelity models. The new algorithm allows for easy image generation based on new trajectories and the asteroid's orientation, spin, and shape. Figure 3b depicts the new visible edge finding technique on the same image of Eros depicted in Fig. 3a. The new boundary finding routine assumes a complete knowledge of the truth is available to generate the visible edge. Thus, the new boundary finding technique is used only for simulation purposes as it is a quicker alternative for image generation than the Blender software.

The measurement equation is based on a pinhole camera, where three-dimensional, discrete points along the visible edge are non-linearly mapped to a two-dimensional image according to:

$$\begin{bmatrix} x_j \\ y_j \\ z_j \end{bmatrix} = \boldsymbol{s} = \boldsymbol{T}_C^I \left[\boldsymbol{T}_I^A \boldsymbol{r}_{e_j/a}^A - \boldsymbol{r}_{s/a}^I \right], \tag{16}$$

$$\boldsymbol{h}(\boldsymbol{x}) = \begin{bmatrix} u_j \\ v_j \end{bmatrix} = \boldsymbol{M}\boldsymbol{\rho}(\boldsymbol{s}) = \boldsymbol{M} \begin{bmatrix} -x_j/z_j \\ y_j/z_j \\ 1 \end{bmatrix}, \tag{17}$$

where $\boldsymbol{M}$ denotes a linear mapping corresponding to the pinhole camera, $\boldsymbol{r}_{s/a}^I$ the relative position of the spacecraft with respect to the asteroid in the inertial frame, $\boldsymbol{r}_{e/a}^A$ the position of a visible edge point relative to the asteroid in the asteroid fixed frame, $\boldsymbol{T}_C^I$ the rotation matrix from the inertial frame to the camera frame, and $\boldsymbol{T}_I^A$ the rotation matrix from the asteroid frame to the inertial frame.

The measurement partials $\boldsymbol{H_r}$, $\boldsymbol{H}_\alpha$, $\boldsymbol{H}_\delta$, $\boldsymbol{H}_{\dot\theta}$, and $\boldsymbol{H}_{\theta_0}$ in previous work[12,14] were calculated with complex step numerical differentiation,[26] but have since been replaced with analytical terms. The analytic partials require multiple levels of chain rule implementation, and the exact expressions are not reported here. The partials with respect to the basis radii $\boldsymbol{H}_{\boldsymbol{f}'}$ are relatively straightforward, and when analyzed with the chain rule also produce the required $\boldsymbol{H_f}$ term. The partials with respect to the basis radii are

$$\frac{\partial \boldsymbol{h}}{\partial \boldsymbol{f}'} = \frac{\partial \boldsymbol{h}}{\partial \boldsymbol{f}}\frac{\partial \boldsymbol{f}}{\partial \boldsymbol{f}'}, \tag{18}$$

where $\frac{\partial \boldsymbol{h}}{\partial \boldsymbol{f}}$ is further broken up such that

$$\frac{\partial \boldsymbol{h}}{\partial \boldsymbol{f}} = \boldsymbol{M}\frac{\partial \boldsymbol{\rho}}{\partial \boldsymbol{s}}\frac{\partial \boldsymbol{s}}{\partial \boldsymbol{f}}, \tag{19}$$

$$\frac{\partial \boldsymbol{h}}{\partial \boldsymbol{f}} = \boldsymbol{M}\frac{\partial \boldsymbol{\rho}}{\partial \boldsymbol{s}}\boldsymbol{T}_C^I\boldsymbol{T}_I^A\hat{\boldsymbol{e}}^A. \tag{20}$$

The partial of a measured radii with respect to the basis radii comes from the GP update equation and is simply

$$\frac{\partial \boldsymbol{f}}{\partial \boldsymbol{f}'} = \boldsymbol{C}(\hat{\boldsymbol{e}}, \hat{\boldsymbol{e}}')\boldsymbol{C}^{-1}(\hat{\boldsymbol{e}}', \hat{\boldsymbol{e}}'). \tag{21}$$

The measurement equation does not depend on velocity, resulting in $\boldsymbol{H_v} = \boldsymbol{0}$.

Data Association

As described previously, the data taken directly from the simulated imagery cannot be directly implemented into the filter. Recall that the GP filter truth shape modeled by the 312 basis nodes is a low fidelity representation of a real asteroid. As such, measurements extracted from the images need to be associated to points that correspond to the visible edge of the GP filter truth shape. This is done to show how real-world data can be associated to data along a lower fidelity filter model, just as real-time gravitational accelerations are represented with finite spherical harmonic expressions. Through data association, the truth filter measurements produced are equivalent to hypothetical image data taken of the low fidelity GP filter truth shape in Fig. 2.

The data association procedure is run on each image data point to generate filter truth measurements. The discrepancy between the image data and the filter truth measurements is caused by differences in the shapes, not the other state elements (the filter truth states are equivalent to the true states). As such, the truth filter measurements can be found by searching along the plane defined by the two unit vectors of $(\boldsymbol{r}^I_{s/a}, \boldsymbol{r}^I_{e_j/s})$.

The unit vector of $\boldsymbol{r}^I_{s/a}$ is rotated in the search plane by a rotation angle γ to optimize the objective function[14]

$$J(\gamma) = \frac{-f(\gamma)||\boldsymbol{r}^I_{s/a}||\sin(\gamma)}{\sqrt{f^2(\gamma) + ||\boldsymbol{r}^I_{s/a}||^2 - 2f(\gamma)||\boldsymbol{r}^I_{s/a}||\cos(\gamma)}}. \tag{22}$$

The resulting position vector is input into Eq. 16 as $\boldsymbol{r}^A_{e/a}$. Figure 4 depicts the results of the data association for the image shown previously in Fig. 3a and Fig. 3b. The data points in red represent the visible edge of Eros' true shape. The data points in blue are those obtained from the data association. Note the difference is small, as the true shape and the GP filter truth model are similar. Furthermore, if simulated imagery were available of the GP filter truth shape, the new image data would yield the same data points in blue. For simulation purposes, new imagery could be generated and the data association process described could be avoided. However, for potential missions where real-time images are taken of a central body, the data association procedure outlined is necessary.

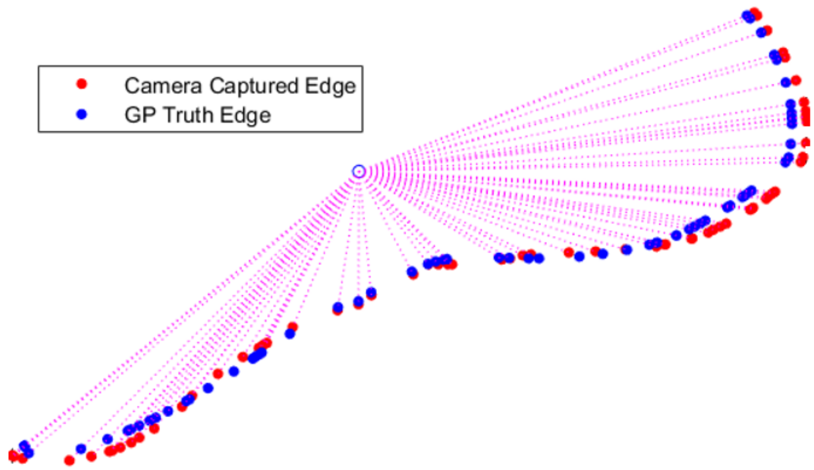

Figure 4: Data Association

The GP batch filter now requires a set of estimated measurements. While it is possible to simulate imagery and obtain the visible edge of the estimated GP shape, each discrete estimated measurement point must correspond to a specific truth measurement point. As there is no clear way to establish a correspondence, the estimated measurements are obtained through the same data association procedure.

The data association procedure is run to generate estimated measurements $\hat{\boldsymbol{z}}$ using the estimated state. A new search plane is defined using the unit vector defined by the estimated state and the unit vector obtained from the image data ($\hat{\boldsymbol{r}}^I_{s/a}, \boldsymbol{r}^I_{e_j/s}$). The unit vector of $\hat{\boldsymbol{r}}^I_{s/a}$ is rotated in the plane to minimize

$$J(\gamma) = \frac{-\hat{f}(\gamma)||\hat{\boldsymbol{r}}^I_{s/a}||\sin(\gamma)}{\sqrt{\hat{f}^2(\gamma) + ||\hat{\boldsymbol{r}}^I_{s/a}||^2 - 2\hat{f}(\gamma)||\hat{\boldsymbol{r}}^I_{s/a}||\cos(\gamma)}}. \tag{23}$$

The only difference between Eq. 22 and Eq. 23 is the use of the estimated state. Thus a discrete set of estimated measurements $\hat{\boldsymbol{z}}$ is obtained that corresponds to each truth measurement in $\boldsymbol{z}$.

The data association limits its optimization to a planar search as described in Eqs. 22 and 23. The planar assumption is valid for the data association to the GP filter truth in Eq. 22, since the remaining truth state elements are identical to those used to produce the camera images. The planar assumption is incorrect for the estimated data association, as the estimated state elements differ from those used to produce the camera images. While this simplification is recognized as a source of error within the filter, the data association is shown to be sufficient for state convergence provided the estimated state does not differ drastically from the truth state. Future work will account for data association error by considering the input nodes with random disturbances.[27,28]

SIMULATION DESIGN AND FILTER SETUP

The GP batch filter is run on four asteroids: Lutetia, Eros, Toutatis, and Bennu. These four are selected based on their interesting shapes and varying masses. For each asteroid, the GP batch filter is run on a hyperbolic approach trajectory and a circular orbit. Each trajectory processes an image of the central body at 30 minute intervals, and takes a total of 104 images. The size of the circular orbits are designed such that the measurement set corresponds to one complete revolution. The hyperbolic trajectories have the same number of measurements, with their end intersecting the circular orbits. Figure 5 depicts the hyperbolic approach and the circular orbit used for Eros in the Body-Fixed frame.

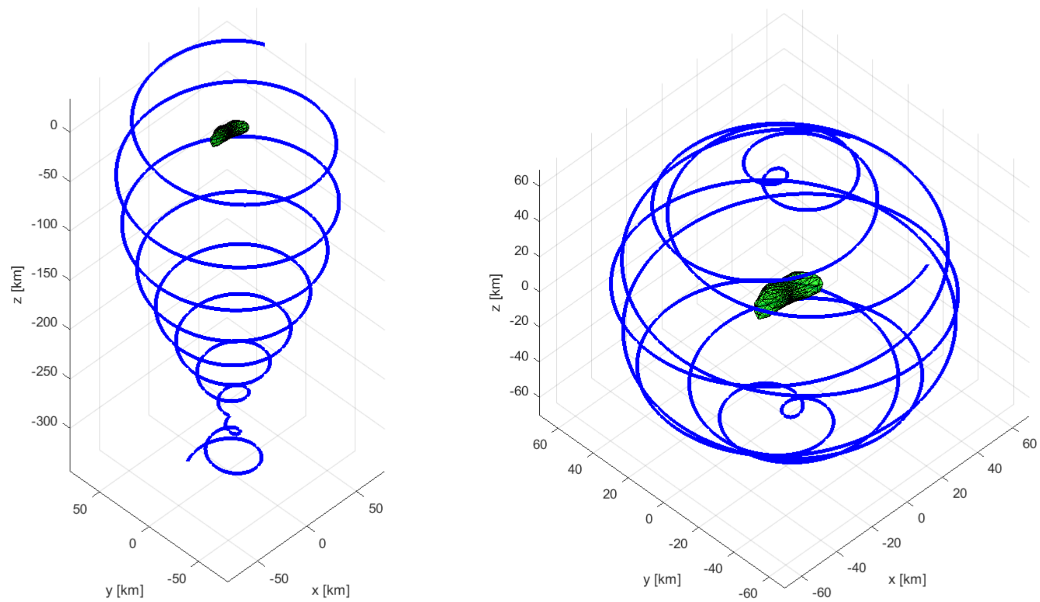

(a) Hyperbolic Approach to Eros

(b) Circular Orbit about Eros

Figure 5: Body Fixed Trajectories

Table 1 depicts the gravitational parameter, spin, and pole orientation values used as the truth in the batch filter. The gravitational parameters and spin rate are obtained from NASA's Planetary Data System,[29] whereas the pole values are all the same as those used by Hollenberg.[14] The spin is assumed to be about a single axis starting at the prime meridian.[19]

Table 1: Asteroid Truth Simulation Data

Asteroid	$\mu \left[\frac{\text{km}^3}{\text{s}^2}\right]$	$\dot{\theta} \left[\frac{\text{deg}}{\text{hr}}\right]$	α [deg]	δ [deg]	θ_0 [deg]
Lutetia	1.1339×10^{-1}	44.07	0	60	-27
Eros	3.9206×10^{-4}	68.31	0	60	-27
Toutatis	1.2673×10^{-6}	116.15*	0	60	-27
Bennu	4.8691×10^{-9}	84.19	0	60	-27

Toutatis' spin is actually 2.77 degrees per hour according NASA,[29] but for this study is modeled at 116.15.

The primary complication of the batch filter is that all measurements are weighted equally over time. In reality, later measurements are taken when the estimate deviates more from the truth and has potentially left the region of linearization. With no prior information, adaptive measurement weighting effective in a sequential filter, such as Lear's method,[14,30,31] is not applicable.

To ensure early batch iterations do not update the state beyond reason and negatively impact later iterations, an alternative measurement underweighting scheme is introduced in the form of an adjusting measurement noise strength.[31] Earlier batch iterations have artificially inflated measurement covariances, effectively adjusting the sensitivity of the batch. This measurement under-weighting is decreased over batch iterations from $\sigma_\epsilon = [1 \times 10^8, 1]$. Note that the truth measurements are not perturbed based on these errors, simply the weights applied with Eq. 9. This technique provides an alternative to other step size control methods[32,33] and ensures that issues with linearization are minimized as the estimate is forced to approach the truth slowly.

Each simulation has an initial estimate perturbed from the truth such that $\hat{\boldsymbol{x}}_0(t_0) = \boldsymbol{x}(t_0) + \Delta\boldsymbol{x}$, where $\Delta\boldsymbol{x}$ are set values chosen to ensure batch convergence. The values presented for $\Delta\boldsymbol{x}$ are based on the largest converging case from various test cases of the GP batch filter, not instances of an initial covariance.

Tables 2 and 3 show the initial perturbations for each asteroid on hyperbolic approach and in circular orbit. Note that the initial perturbations on the initial position and velocity are larger for more massive asteroids. Also note that while the initial velocity and spin errors are small, the approach trajectory lasts 52 hours, causing large offsets at the trajectory's end. Furthermore, the initial position and velocity perturbations in circular orbit are much smaller than the hyperbolic approach. On approach, the asteroid is illuminated almost entirely for most of the trajectory; the lighting conditions for a circular orbit change from fully illuminated to fully eclipsed, resulting in less data collected while in a circular orbit. The perturbations to θ_0 are small, as previous work indicates that θ_0 may not be fully observable with silhouette-based measurements. As such, the initial perturbations are small to ensure the estimate does not drift to far from the truth.

Table 2: Hyperbolic Approach: Initial State Perturbation

Perturbation	Lutetia	Eros	Toutatis	Bennu
$\Delta\boldsymbol{r}$	2 km	1 km	250 m	10 m
$\Delta\boldsymbol{v}$	2 mm/s	1 mm/s	0.1 mm/s	0.01 mm/s
$\Delta\alpha$, $\Delta\delta$	$5°$	$5°$	$5°$	$5°$
$\Delta\dot{\theta}$	$0.5°$/hr	$0.5°$/hr	$0.5°$/hr	$0.5°$/hr
$\Delta\theta_0$	$0.1°$	$0.1°$	$0.1°$	$0.1°$

Table 3: Circular Orbit: Initial State Perturbation

Perturbation	Lutetia	Eros	Toutatis	Bennu
$\Delta\boldsymbol{r}$	650 m	100 m	25 m	5 m
$\Delta\boldsymbol{v}$	1 mm/s	1 mm/s	0.1 mm/s	0.005 mm/s
$\Delta\alpha$, $\Delta\delta$	$5°$	$5°$	$5°$	$5°$
$\Delta\dot{\theta}$	$0.5°$/hr	$0.5°$/hr	$0.5°$/hr	$0.5°$/hr
$\Delta\theta_0$	$0.1°$	$0.1°$	$0.1°$	$0.1°$

The initial shape estimate for each asteroid is a large ellipsoid. Ellipsoids were chosen to represent a fair estimate of the asteroid's size without representing the finer aspects of the asteroid's shape. The initial shape estimates are ($60\times65\times45$ km) for Lutetia, ($18\times9\times8$ km) for Eros, ($1.5\times1.5\times2.25$ km) for Toutatis, and ($0.3 \times 0.3 \times 0.3$ km) for Bennu. Figure 6 depicts the truth GP Truth Shape and the initial GP Estimate for Lutetia.

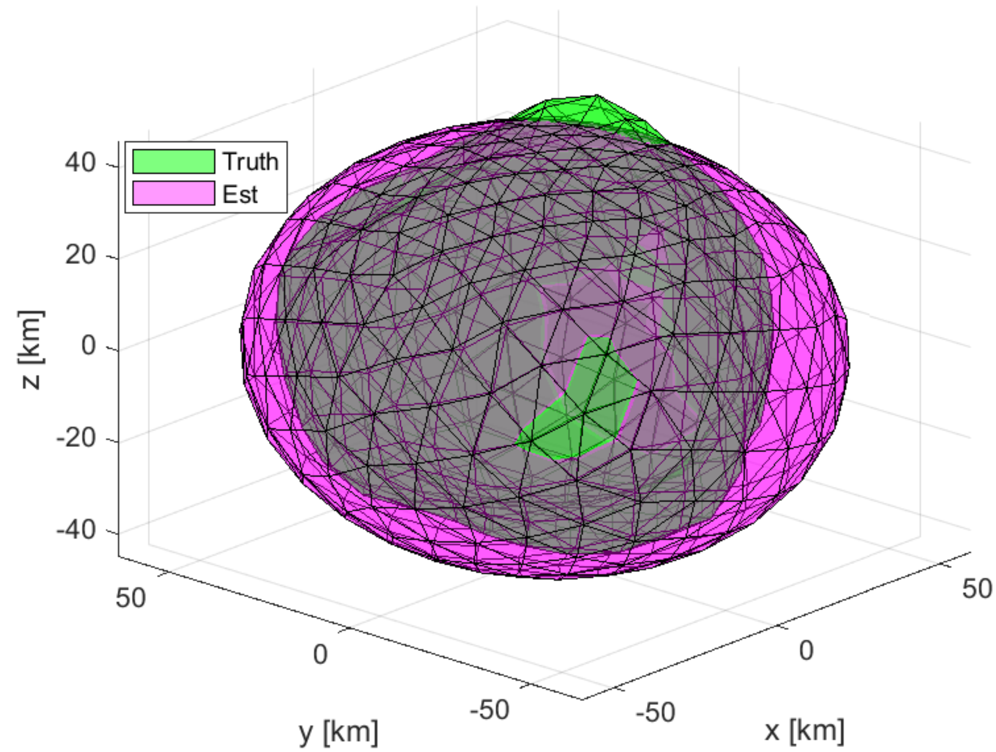

Figure 6: Lutetia ($60 \times 65 \times 45$ km)

It is important here to address the limitations of the GP batch filter and the extent of its testing in the framework of this research's objectives. Given the sensitivity to initial errors that the GP batch filter faces, it would be wise to consider estimating the state on a trajectory with a shorter time, or subdividing the batch into sub-intervals and implementing a sliding batch. However, the primary purpose of this work is obtain a covariance matrix with variances and spacial correlations appropriate to perturb the truth in future Monte Carlo studies. As such, longer time trajectories are necessary to ensure that the entire asteroid is observed and sufficient data collected. Furthermore, the concern of observability already exists with the entire measurement set, and earlier state estimation may require a smaller diffuse prior, weakening the maximum likelihood assumption.

It is also recognized that the GP batch filter is tested on a limited set of initial perturbations. Sensitivity studies where the initial state perturbations $\Delta \boldsymbol{x}$ are sampled randomly from an initial covariance are performed, but with very few individual samples and thus not reported. As the primary purpose of the batch filter is to obtain initial estimates and covariances for future Monte Carlo studies, extensive sensitivity studies are not performed.

FILTER RESULTS

Approach Results

The residuals from the batch filter are recorded at the final time according to $\boldsymbol{x}(t_f) - \hat{\boldsymbol{x}}_i(t_f)$. Note that the residuals for the asteroid shape, pole, and spin are constant through time as they are static states. For ease of comparison across asteroid scenarios, the relative errors ϵ are recorded for the position, velocity, and shape at each batch iteration $\boldsymbol{i}$ according to

$$\epsilon_{ir}(t_f) = \frac{||\boldsymbol{r}(t_f) - \hat{\boldsymbol{r}}_i(t_f)||}{\boldsymbol{r}(t_f)}, \tag{24}$$

$$\epsilon_{iv}(t_f) = \frac{||\boldsymbol{v}(t_f) - \hat{\boldsymbol{v}}_i(t_f)||}{\boldsymbol{v}(t_f)}, \tag{25}$$

$$\epsilon_{i'f}(t_f) = \frac{||\boldsymbol{f}'(t_f) - \hat{\boldsymbol{f}}'_i(t_f)||}{\boldsymbol{f}(t_f)}. \tag{26}$$

All radii are combined into one error metric for simplicity. The pole and spin states are presented as absolute residuals, as the magnitude of the residuals are comparable between asteroids.

Figure 7a depicts the relative shape errors from the batch filter on approach to the four asteroids. The results indicate that while each asteroid starts with roughly the same relative error, Bennu performs the worst and Toutatis performs the best. It is not uncommon for relative errors to increase slightly, as Toutatis does around iteration 16. These increases are attributed to multi-state estimation and the adjusting measurement underweighting. For example, one radii estimate may approach the truth, but the iteration's correlations between radii are inaccurate, causing nearby radii to drift away from the truth. Another instance of error increase is seen for Eros at iteration 18. Eros has large craters on its upper and lower side that are not directly observable with silhouette-based measurements. Only the spatial correlations help craters converge to the truth. As a result, these radii have larger estimation variances. The slight upward trend of Eros near the end of the batch iteration is attributed to the crater estimates changing slightly within their variance bounds.

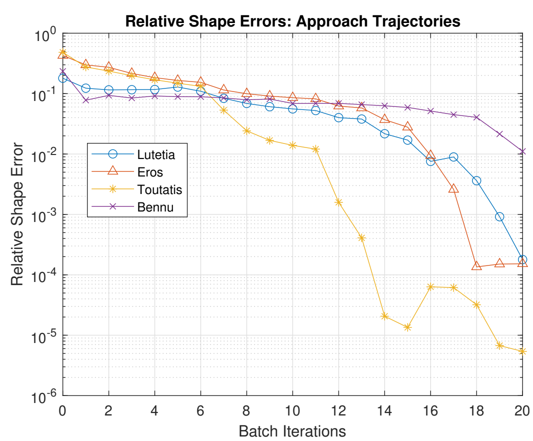

(a) Total Radii Relative Error: Approach

Figure 8 depicts the remaining state errors along the approach trajectory towards the four asteroids. It is clear that estimation about Bennu is more difficult than the other asteroids; it is hypothesized that the poor estimation performance is due to Bennu's spherical shape and lack of distinguishing geographical features. Also note that the prime meridian does not converge despite having a small initial perturbation, further indicating the state element may not be observable. Furthermore, the prime meridian of Bennu diverges rather dramatically compared to the other asteroids.

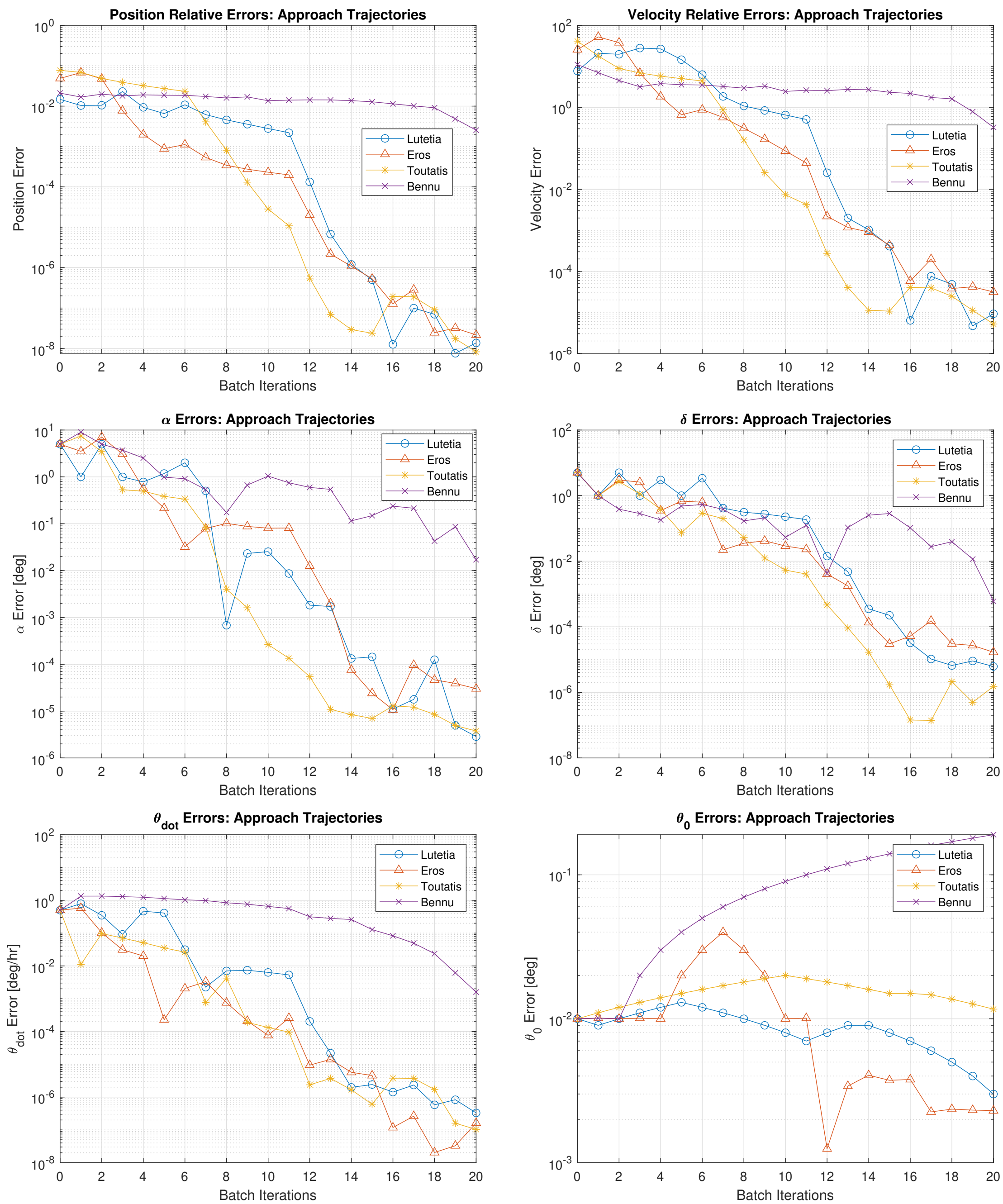

Figure 8: Approach Trajectory State Errors

Bennu Shape Alterations

The comparatively poor performance of the filter on approach to Bennu is hypothesized to be caused by Bennu's near-spherical shape. To test this hypothesis, an additional batch simulation is run where two of the truth radii of Bennu are increased by 25%, creating large mountain-like structures as depicted in Fig. 9

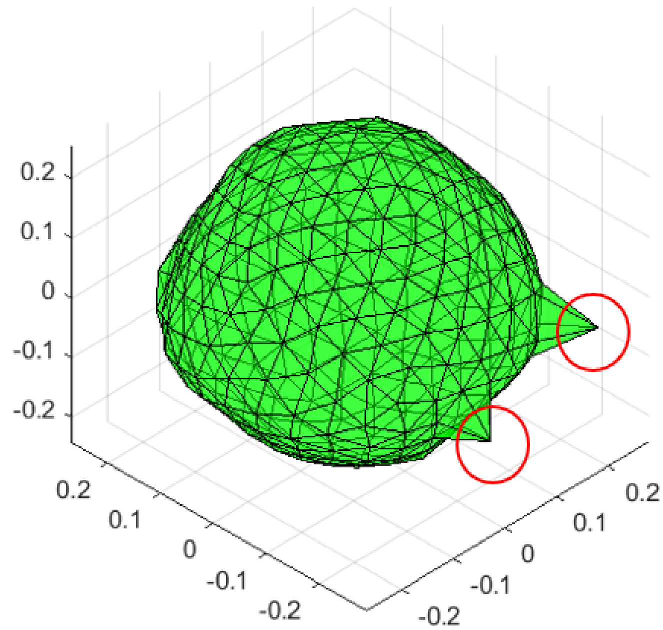

Figure 9: Altered Bennu Shape

Rerunning the filter with measurement data generated on the altered shape yielded in smaller relative errors in the shape estimation, as seen in Fig. 10a. The new relative shape errors are now similar with those of Lutetia and Eros.

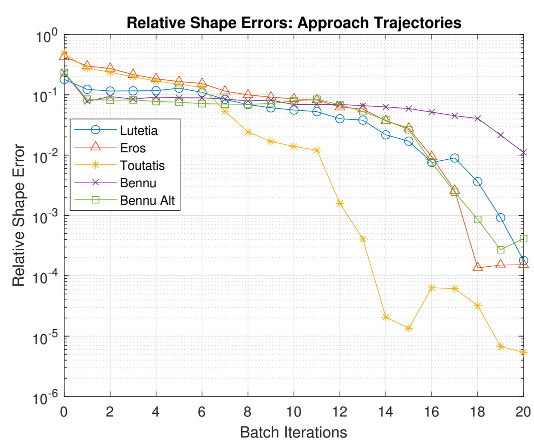

(a) Total Radii Relative Error: Altered Bennu

Furthermore, the altered shape yielded smaller errors for all states, as seen in Fig. 11. Particular improvement occurred in position, velocity, spin, and prime meridian errors, with a slight improvement for the right ascension and declination.

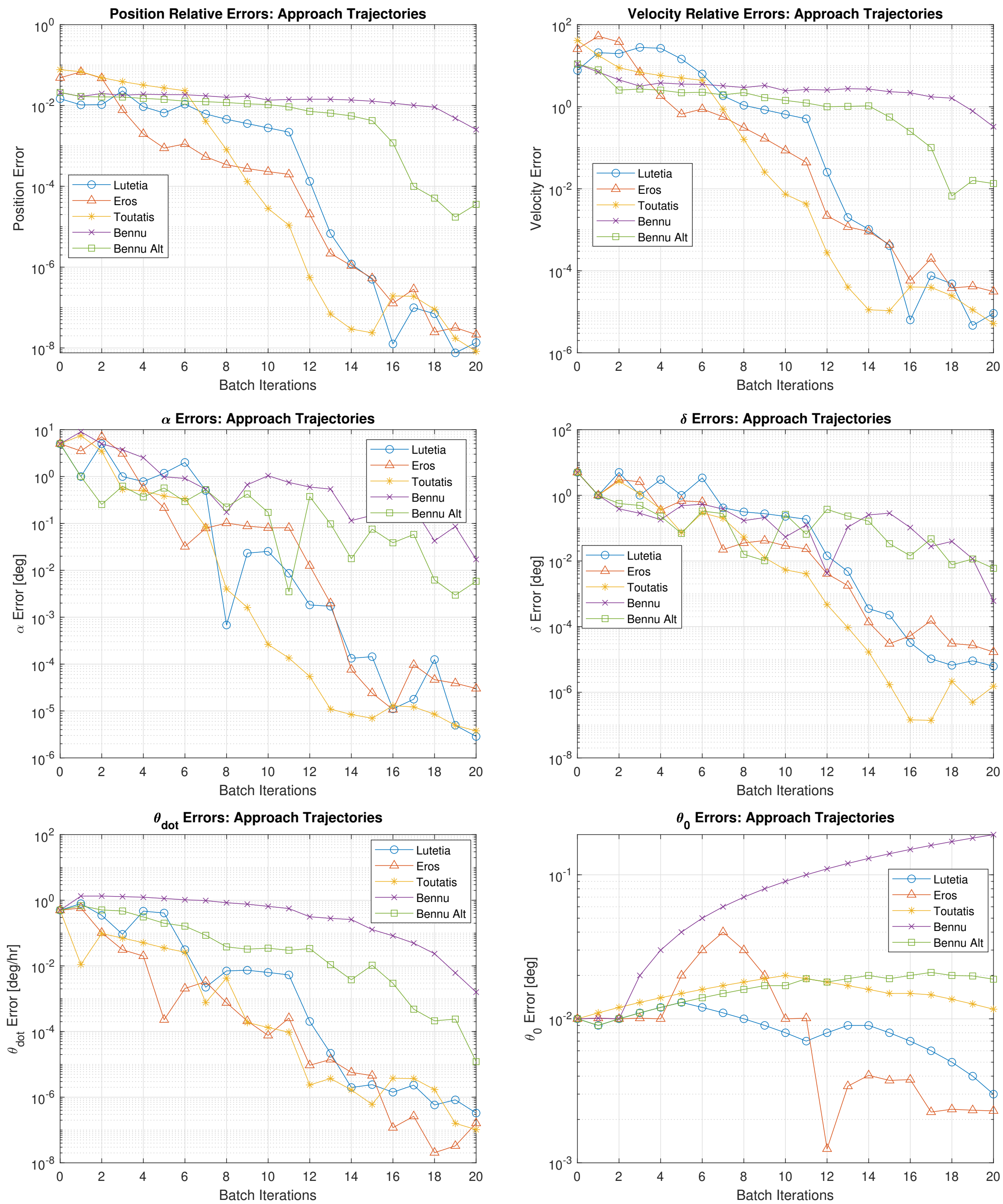

Figure 11: Approach Trajectory State Errors: Altered Bennu

Circular Orbit Results

Figure 12a depicts the relative shape errors from the batch filter in circular orbit about the four asteroids. Note that unlike the approach results, all asteroids do comparatively well. The comparative performance is most likely due to the circular orbit seeing more geometry of the central body than the approach trajectory. Furthermore, the initial errors in circular orbit are smaller than approach, helping the results converge across scenarios.

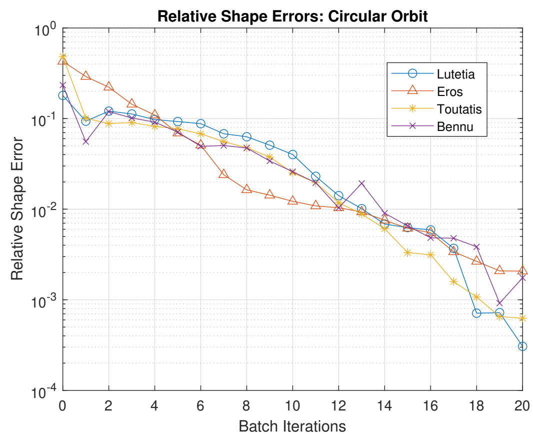

(a) Total Radii Relative Error: Circular Orbit

Figure 13 depicts the relative position and velocity errors in circular orbit. The results clearly depict that the position and velocity is best estimated about Eros.

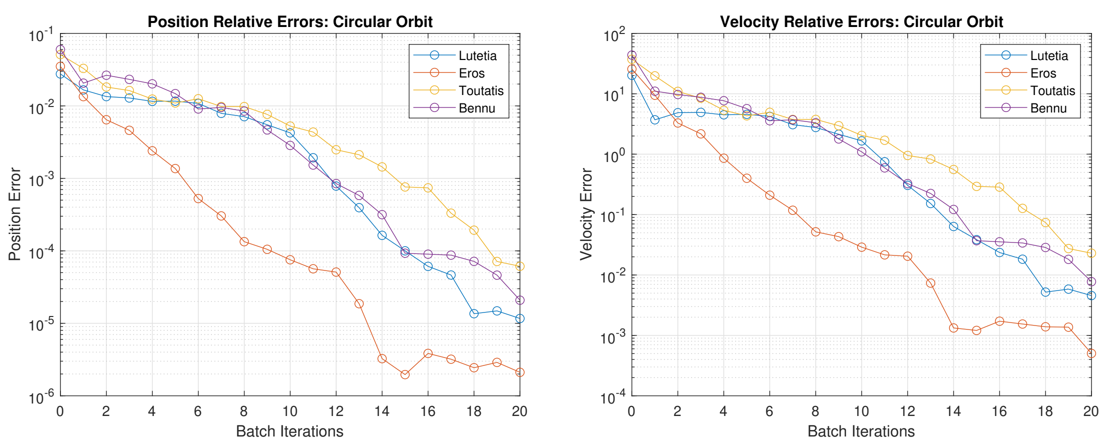

Figure 13: Circular Orbit: Position and Velocity Relative Errors

Lastly, Fig. 14 depicts the pole and spin errors in circular orbit. Once again Bennu has the worst pole and spin estimation, but like the shape errors, is more comparable to the other asteroids. It is also clear that the prime meridian does not converge to the truth, further pointing to observability issues.

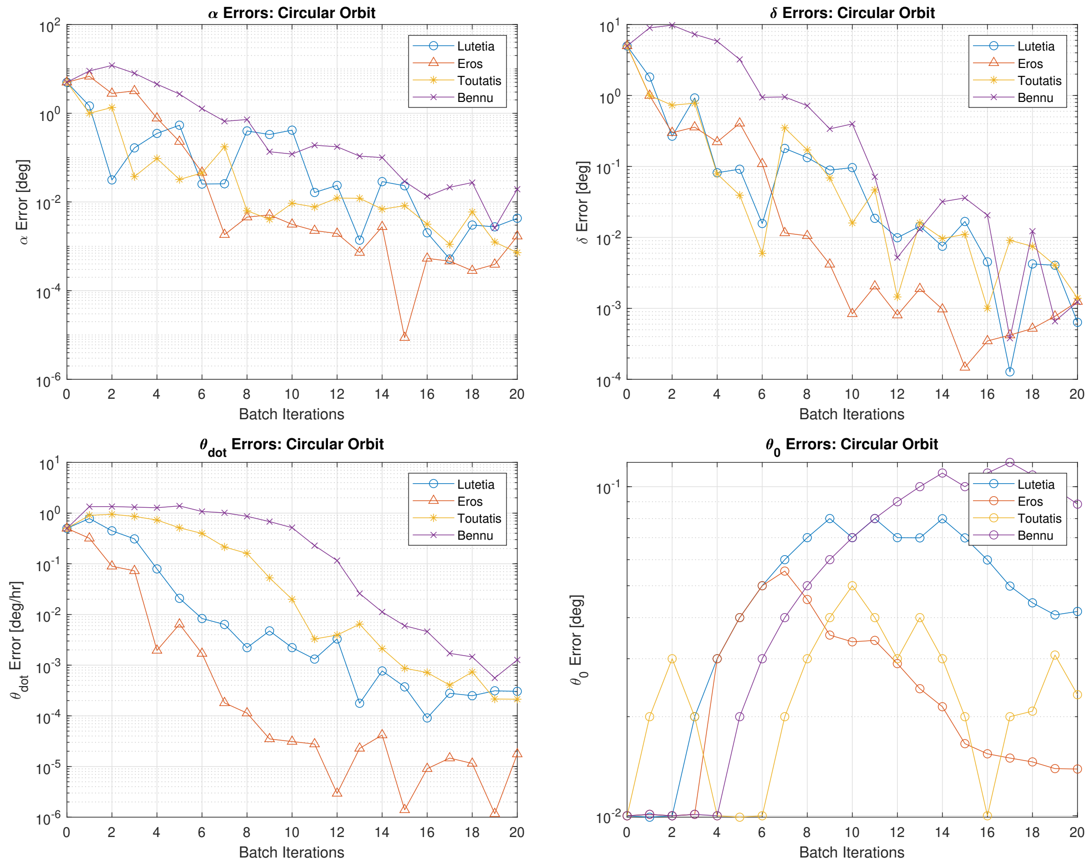

Figure 14: Circular Orbit: Pole and Spin Errors

Results Discussion and Shape Covariances

An interesting result is that Eros outperforms the other asteroids in circular orbit, but not on approach. Eros' better filter convergence is most likely due to the initial perturbation applied to Eros being comparatively smaller than the other asteroids, but may be indicative that the spin and shape of Eros yield better estimation results in circular orbit. Bennu also performed far better in circular orbit than on approach, again attributed to the significantly smaller initial perturbation (specifically velocity) applied to Bennu compared to the other asteroids.

Recall that these results are from a single set of initial perturbations. Generalizing these results to broader conclusions on the comparative performance between asteroids and trajectories should be done sparingly. As stated, a primary goal of the GP batch filter is to obtain a statistically consistent covariance of the shape estimate, unbiased by initial information. The covariance from the last iteration of the approach trajectory to Eros was pulled and used to perturb the truth. Figure 15 depicts a random perturbation pulled normally from the covariance and used to perturb Eros, with the perturbed shape in red and the original in green.

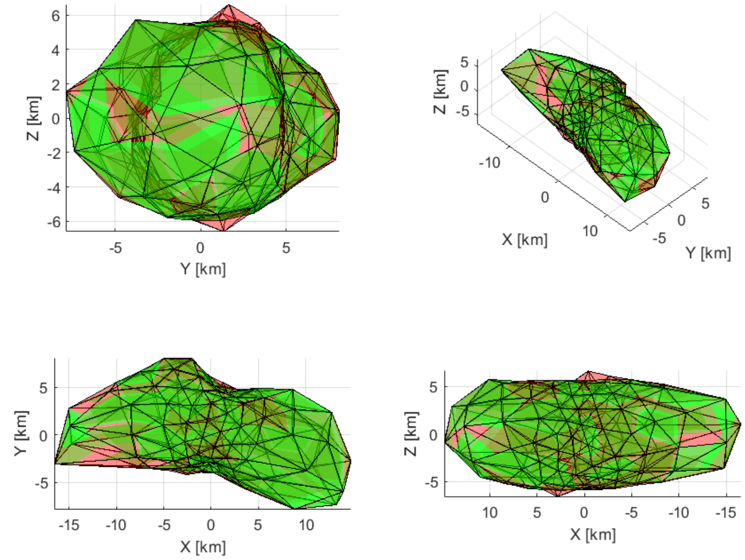

Figure 15: Truth Shape Perturbations

The final covariances have been obtained from the batch filter and are ready to be used as initial shape perturbations for a complete Monte Carlo analysis. The Monte Carlo analyses consist of running numerous, Gaussian disturbances of the state (position, velocity, pole, spin, and shape) to formulate new truth states, where an IEKF estimates each new truth. Future work will present the results of the Monte Carlo analysis and steps taken to improve the IEKF filter. The filter is expected to improve with a robust measurement rejection scheme[34] that ensures the shape estimate does not deviate too far from the truth. Furthermore, issues with the data association to the estimated shape are to be mitigated through input noise incorporation as described in Mchutchon[27] and Johnson.[28]

CONCLUSION

Results from the GP batch filter demonstrate its ability to simultaneously estimate the observing spacecraft's position and velocity and the central body's orientation, spin, and shape. The GP batch filter successfully estimated the augmented state of bodies with various shapes and sizes: Lutetia, Eros, Toutatis, and Bennu. With the multi-iteration adjusting measurement weight scheme, the filter is able to take large ellipsoidal initial shape estimates and converge to the truth.

The primary goal of obtaining initial state estimates and covariances for perturbing the truth states in a Monte Carlo analysis is complete. Future work will focus on large Monte Carlo studies using an IEKF to study the performance of the sequential GP filter for various SLAM applications. Future work on the filter itself includes a sliding batch filter, where subsets of the trajectory are analyzed and state estimates made earlier along the trajectory.

ACKNOWLEDGEMENTS

This research was carried out at The University of Texas at Austin, funded by the Jet Propulsion Laboratory, California Institute of Technology, under Research Support Agreement 1704630, and at the Jet Propulsion Laboratory, California Institute of Technology, under a contract with the National Aeronautics and Space Administration.

REFERENCES

[1] R. Gaskell, O. Barnouin-Jha, D. J. Scheeres, A. Konopliv, T. Mukai, S. Abe, J. Saito, M. Ishiguro, T. Kubota, T. Hashimoto, *et al.*, "Characterizing and navigating small bodies with imaging data," *Meteoritics & Planetary Science*, Vol. 43, No. 6, 2008, pp. 1049–1061, https://doi.org/10.1111/j.1945-5100.2008.tb00692.x.

[2] O. Barnouin, R. Gaskell, E. Kahn, C. Ernst, M. Daly, E. Bierhaus, C. Johnson, B. Clark, and D. Lauretta, "Assessing the quality of topography from stereo-photoclinometry," *Asteroids, Comets, Meteors 2014*, 2014, p. 28, 2014acm..conf...28B.

[3] M. Perry, O. Barnouin, M. Daly, J. Seabrook, E. Palmer, R. Gaskell, K. Craft, J. Roberts, L. Philpott, M. A. Asad, *et al.*, "The global topography of Bennu: altimetry, photoclinometry, and processing," *European Planetary Science Congress*, 2017, pp. EPSC2017–952, 2017EPSC...11..952P.

[4] R. Park, A. Vaughan, A. Konopliv, A. Ermakov, N. Mastrodemos, J. Castillo-Rogez, S. Joy, A. Nathues, C. Polanskey, M. Rayman, *et al.*, "High-resolution shape model of Ceres from stereophotoclinometry using Dawn imaging data," *Icarus*, Vol. 319, 2019, pp. 812–827, https://doi.org/10.1016/j.icarus.2018.10.024.

[5] R. Gaskell, O. Barnouin, M. Daly, E. Palmer, J. Weirich, C. Ernst, R. Daly, and D. Lauretta, "Stereophotoclinometry on the OSIRIS-REx Mission: mathematics and Methods," *The Planetary Science Journal*, Vol. 4, No. 4, 2023, p. 63, 10.3847/PSJ/acc4b9.

[6] N. Takeishi, T. Yairi, Y. Tsuda, F. Terui, N. Ogawa, and Y. Mimasu, "Simultaneous estimation of shape and motion of an asteroid for automatic navigation," *2015 IEEE International Conference on Robotics and Automation (ICRA)*, IEEE, 2015, pp. 2861–2866, 10.1109/ICRA.2015.7139589.

[7] B. Bercovici and J. W. McMahon, "Robust autonomous small-body shape reconstruction and relative navigation using range images," *Journal of Guidance, Control, and Dynamics*, Vol. 42, No. 7, 2019, pp. 1473–1488, https://doi.org/10.2514/1.G003898.

[8] K. Kuppa, J. W. McMahon, and A. B. Dietrich, "Initial Pole Axis and Spin Direction Estimation of Asteroids Using Infrared Imagery," *Journal of Guidance, Control, and Dynamics*, Vol. 47, No. 6, 2024, pp. 1055–1071, https://doi.org/10.2514/1.G007736.

[9] J. W. McMahon and D. J. Scheeres, "Shape estimation from lightcurves including constraints from orbit determination," *Advanced Maui Optical and Space Surveillance Technologies Conference*, 2016, p. 56, 2016amos.confE..56M.

[10] D. Baker and J. W. McMahon, "Shape and Pole Estimation for Small-Bodies on Approach," *AIAA SCITECH 2022 Forum*, 2022, p. 2382, https://doi.org/10.2514/6.2022-2382.

[11] N. Wahlström and E. Özkan, "Extended target tracking using Gaussian processes," *IEEE Transactions on Signal Processing*, Vol. 63, No. 16, 2015, pp. 4165–4178, 10.1109/TSP.2015.2424194.

[12] E. M. Zucchelli, B. A. Jones, and R. P. Russell, "Pose and Shape Estimation of a Small Body Via Extended Target Tracking," *American Astronautical Society, Astrodynamics Specialist Conference*, 2019, pp. 19–678.

[13] E. M. Zucchelli, N. Lifset, B. A. Jones, R. P. Russell, and S. Bhaskaran, "Towards Limb-Based Autonomous Navigation and Mapping of Primitive Bodies," *American Astronautical Society, Astrodynamics Specialist Conference*, 2022, pp. 22–644.

[14] C. Hollenberg, "Horizon-based autonomous navigation and mapping for small body missions," *Univeristy of Texas Libraries*, 2023.

[15] P. S. Maybeck, *Stochastic models, estimation, and control*. Academic press, 1982.

[16] C. E. Rasmussen and H. Nickisch, "Gaussian processes for machine learning (GPML) toolbox," *The Journal of Machine Learning Research*, Vol. 11, 2010, pp. 3011–3015.

[17] B. Clark, A. Sen, X.-D. Zou, D. Dellagiustina, S. Sugita, N. Sakatani, M. Thompson, D. Trang, E. Tatsumi, M. Barucci, *et al.*, "Overview of the search for signs of space weathering on the low-albedo asteroid (101955) Bennu," *Icarus*, 2023, p. 115563, https://doi.org/10.1016/j.icarus.2023.115563.

[18] C. W. Hergenrother, M. C. Nolan, R. P. Binzel, E. A. Cloutis, M. A. Barucci, P. Michel, D. J. Scheeres, C. D. d'Aubigny, D. Lazzaro, N. Pinilla-Alonso, *et al.*, "Lightcurve, color and phase function photometry of the OSIRIS-REx target asteroid (101955) Bennu," *Icarus*, Vol. 226, No. 1, 2013, pp. 663–670, https://doi.org/10.1016/j.icarus.2013.05.044.

[19] R. S. Hudson and S. J. Ostro, "Shape and non-principal axis spin state of asteroid 4179 Toutatis," *Science*, Vol. 270, No. 5233, 1995, pp. 84–86, 10.1126/science.270.5233.84.

[20] R. Gaskell, "Gaskell Eros shape model V1. 0," *NASA Planetary Data System*, 2008, pp. NEAR–A, 2008PDSS...92.....G.

[21] B. Carry, M. Kaasalainen, W. J. Merline, T. G. Müller, L. Jorda, J. D. Drummond, J. Berthier, L. O'Rourke, J. Ďurech, M. Küppers, *et al.*, "Shape modeling technique KOALA validated by ESA Rosetta at (21) Lutetia," *Planetary and Space Science*, Vol. 66, No. 1, 2012, pp. 200–212, https://doi.org/10.1016/j.pss.2011.12.018.

[22] M. T. Zuber, D. E. Smith, M. M. Watkins, S. W. Asmar, A. S. Konopliv, F. G. Lemoine, H. J. Melosh, G. A. Neumann, R. J. Phillips, S. C. Solomon, *et al.*, "Gravity field of the Moon from the Gravity Recovery and Interior Laboratory (GRAIL) mission," *Science*, Vol. 339, No. 6120, 2013, pp. 668–671, 10.1126/science.1231507.

[23] J. L. Crassidis and J. L. Junkins, *Optimal estimation of dynamic systems*. Chapman and Hall/CRC, 2004.

[24] W.-W. Lin, V. Mehrmann, and H. Xu, "Canonical forms for Hamiltonian and symplectic matrices and pencils," *Linear Algebra and its Applications*, Vol. 302, 1999, pp. 469–533, 10.1016/S0024-3795(99)00191-3.

[25] Blender Online Community, *Blender - a 3D modelling and rendering package*. Blender Foundation, Blender Institute, Amsterdam,

[26] A. R. Campbell, "Numerical analysis of complex-step differentiation in spacecraft trajectory optimization problems," *Texas Digital Commons*, 2011.

[27] A. McHutchon and C. Rasmussen, "Gaussian process training with input noise," *Advances in neural information processing systems*, Vol. 24, 2011.

[28] J. E. Johnson, V. Laparra, and G. Camps-Valls, "Accounting for input noise in Gaussian process parameter retrieval," *IEEE Geoscience and Remote Sensing Letters*, Vol. 17, No. 3, 2019, pp. 391–395, 10.1109/LGRS.2019.2921476.

[29] NASA, "Asteroid Fact Sheet," September 27, 2019.

[30] W. M. Lear, "Multi-phase navigation program for the Space Shuttle Orbiter," *Johnson Spacecraft Center, Houston, Texas, IN*, 1973.

[31] R. Zanetti, K. J. DeMars, and R. H. Bishop, "Underweighting nonlinear measurements," *Journal of guidance, control, and dynamics*, Vol. 33, No. 5, 2010, pp. 1670–1675, https://doi.org/10.2514/1.50596.

[32] D. W. Marquardt, "An algorithm for least-squares estimation of nonlinear parameters," *Journal of the society for Industrial and Applied Mathematics*, Vol. 11, No. 2, 1963, pp. 431–441, https://doi.org/10.1137/0111030.

[33] K. Levenberg, "A method for the solution of certain non-linear problems in least squares," *Quarterly of applied mathematics*, Vol. 2, No. 2, 1944, pp. 164–168.

[34] E. Navon and B. Bobrovsky, "An efficient outlier rejection technique for Kalman filters," *Signal Processing*, Vol. 188, 2021, p. 108164, https://doi.org/10.1016/j.sigpro.2021.108164.